

# Deterministic entanglement of photons in two superconducting microwave resonators

H. Wang,<sup>1,2</sup> Matteo Mariani,<sup>1</sup> Radoslaw C. Bialczak,<sup>1</sup> M. Lenander,<sup>1</sup> Erik Lucero,<sup>1</sup> M. Neeley,<sup>1</sup> A. O'Connell,<sup>1</sup> D. Sank,<sup>1</sup> M. Weides,<sup>1</sup> J. Wenner,<sup>1</sup> T. Yamamoto,<sup>1,3</sup> Y. Yin,<sup>1</sup> J. Zhao,<sup>1</sup> John M. Martinis,<sup>1</sup> and A. N. Cleland<sup>1,\*</sup>

<sup>1</sup>*Department of Physics, University of California, Santa Barbara, CA 93106, USA*

<sup>2</sup>*Department of Physics and Zhejiang California International NanoSystems Institute, Zhejiang University, Zhejiang 310027, China*

<sup>3</sup>*Green Innovation Research Laboratories, NEC Corporation, Tsukuba, Ibaraki 305-8501, Japan*

(Dated: October 11, 2018)

Quantum entanglement, one of the defining features of quantum mechanics, has been demonstrated in a variety of nonlinear spin-like systems. Quantum entanglement in linear systems has proven significantly more challenging, as the intrinsic energy level degeneracy associated with linearity makes quantum control more difficult. Here we demonstrate the quantum entanglement of photon states in two independent linear microwave resonators, creating  $N$ -photon NOON states as a benchmark demonstration. We use a superconducting quantum circuit that includes Josephson qubits to control and measure the two resonators, and we completely characterize the entangled states with bipartite Wigner tomography. These results demonstrate a significant advance in the quantum control of linear resonators in superconducting circuits.

Quantum superposition and entanglement have been demonstrated experimentally using spin-like physical systems ranging from atoms to electronic circuits [1–7]. These systems all display strong nonlinearity, and are used because this nonlinearity allows straightforward quantum control by classical means. The quantum control of linear systems, exemplified by the harmonic oscillator, is by contrast more difficult, and has only been achieved using nonlinear intermediaries: Atoms [1, 8] to control optical cavities, ions to control ion motion [9, 10], and superconducting qubits to control photons in microwave resonators [11–14]. Quantum entanglement of cavity photons still presents a significant challenge: Experiments have demonstrated maximally-entangled photons in different polarization modes of the same cavity [15, 16], but the entanglement of photons in two physically distinct cavities [17–19] has proven more elusive.

Here we show the deterministic generation of entangled photon states in two spatially-separated microwave resonators, achieved by manipulating the photon states with a pair of superconducting phase qubits. We use as a benchmark the generation of NOON states [20–24], comprising a total of  $N$  photons in the two resonators ( $A$  and  $B$ ), entangled in the quantum state

$$|\psi\rangle = \frac{1}{\sqrt{2}}(|N\rangle_A |0\rangle_B + |0\rangle_A |N\rangle_B), \quad (1)$$

with  $N$  photons in resonator  $A$  and zero in  $B$ , superposed with the state with the occupation numbers reversed. Such a state has the same degree of entanglement as the Bell state, but with  $N$  excitations. We also generate MOON states, in which, e.g., resonator  $A$  has  $M$  or zero quanta, entangled with resonator  $B$  with zero or  $N$  quanta. We fully characterize the two-resonator photon states using bipartite Wigner tomography, which represents a non-trivial extension of single-cavity Wigner to-

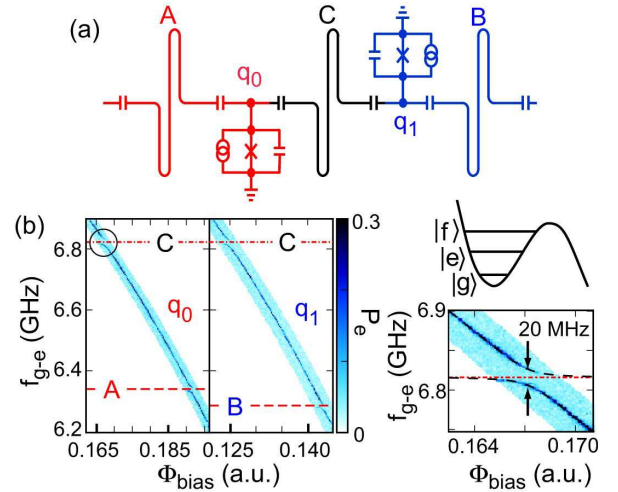


FIG. 1: (Color online) (a) Device circuit schematic. Coupling resonator  $C$  is connected to  $q_0$  and  $q_1$  using 20 MHz coupling capacitors, while storage resonator  $A$  ( $B$ ) is connected to  $q_0$  ( $q_1$ ) through a 17 MHz coupling capacitor. (b) Qubit spectroscopy, showing probability  $P_e$  (color bar) vs. microwave frequency and flux bias for each qubit. Avoided-level crossings near 6.8 GHz (dash-dot lines) are due to the coupling resonator  $C$  and near 6.3 GHz (dashed lines) due to each qubit's storage resonator. Lower right panel shows magnified view of circled area, upper right panel shows three qubit levels.

mography [1, 9, 12–14], and allows us to distinguish entanglement from an incoherent ensemble.

To accomplish this goal, we developed a new quantum circuit comprising two superconducting phase qubits [25] and three microwave resonators. A sketch of the circuit topology is shown in Figs. 1(a). The circuit includes a coupling resonator  $C$ , connected to both qubits, and two state storage resonators  $A$  and  $B$ , each coupled to one qubit. The resonator frequencies are all different

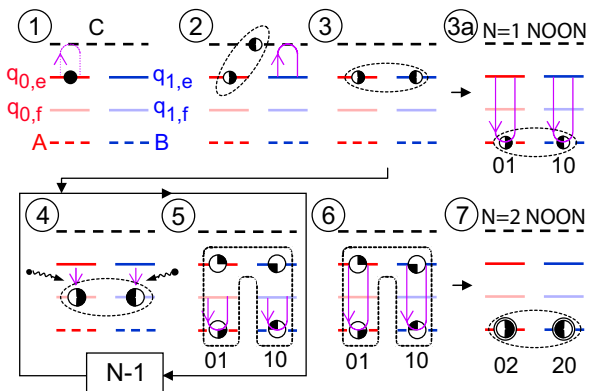


FIG. 2: (Color online) NOON state preparation sequence. Resonators are represented by dashed lines, and the qubit  $|g\rangle \leftrightarrow |e\rangle$  and  $|e\rangle \leftrightarrow |f\rangle$  transitions by dark and light color solid lines, respectively. (1):  $q_0$  is excited to  $|e\rangle$  and half-swapped to  $C$ , generating the Bell state  $|e0\rangle + |g1\rangle$ . (2): Coupling resonator swapped to  $q_1$ , generating  $|eg\rangle + |ge\rangle$ . (3a):  $N = 1$  NOON state  $|10\rangle + |01\rangle$  generated by fully swapping each qubit to its storage resonator. For higher  $N$  states: (4): Qubits excited to  $|fg\rangle + |gf\rangle$ . (5): One photon swapped into storage resonators, generating  $|eg10\rangle + |ge01\rangle$ . Steps (4) and (5) are repeated  $N - 1$  times, generating  $|eg(N - 1)0\rangle + |ge0(N - 1)\rangle$ . (6): Final photon transfer generates (7)  $N = 2$  (or higher  $N$ ) NOON state.

which allows us to frequency-select the qubit-resonator interactions.

The basic method for generating two-resonator entangled states, illustrated in Fig. 2, is to excite and then entangle the two qubits using the coupling resonator. We can swap the resulting Bell state  $|eg\rangle + |ge\rangle$  to the two storage resonators, creating an  $N = 1$  NOON state  $|10\rangle + |01\rangle$ . If we want to generate higher  $N$  photon states, we instead selectively excite each qubit to its next higher energy level  $|f\rangle$  (Fig. 1(b)), generating the state  $|fg\rangle + |gf\rangle$ , thus using the qubits as “qutrits” [26, 27]. The required microwave excitation is selective, due to the anharmonicity of the qubits. The qubit excitation is then swapped to each storage resonator through the qubit  $|f\rangle \leftrightarrow |e\rangle$  transition, creating a four-fold entangled state  $|eg10\rangle + |ge01\rangle$ , where the first two letters indicate the qubit states, and the second two numbers the storage resonator states. We then re-excite the qubits to their  $|f\rangle$  states, and again swap the excitation to the resonators, generating  $|eg20\rangle + |ge02\rangle$ . This process can be repeated until the entangled state has  $N - 1$  photons. In the final step, each qubit’s  $|e\rangle \leftrightarrow |g\rangle$  transition is brought on resonance with the corresponding storage resonator, swapping the last excitation and leaving the system in  $|ggN0\rangle + |gg0N\rangle = |gg\rangle \otimes (|N0\rangle + |0N\rangle)$ , an  $N$ -photon NOON state.

We analyze the final resonator state using the qubits as probes. The simplest analysis uses a coincidence measurement: We bring the qubits into resonance with their

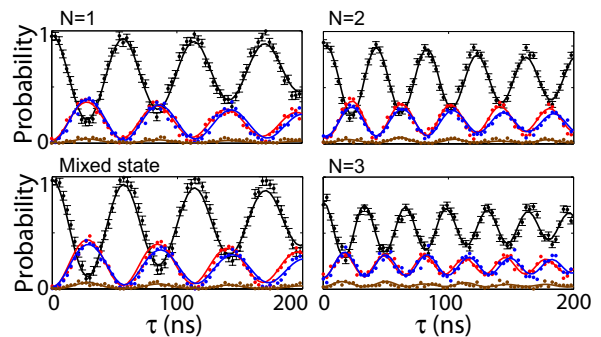


FIG. 3: (Color online) Qubit coincidence probability measurements for  $N = 1, 2$ , and  $3$  NOON states, and for a mixed state.  $P_{ge}$  (blue) and  $P_{eg}$  (red) oscillate with interaction time  $\tau$  at a rate  $\propto \sqrt{N}$ , while  $P_{ee}$  (brown) always remains small. For the mixed state, behavior is nearly identical to the  $N = 1$  NOON state. Lines are fits to the data. Statistical errors, from the measured probability spread of  $\sim 2 - 3\%$ , are shown only for  $P_{gg}$  [30]. Horizontal and vertical axes are same for all plots.

corresponding storage resonators for an interaction time  $\tau$ , after which both qubits are measured simultaneously. The preparation and measurement sequence is repeated  $\sim 10^3$  times, yielding the joint-qubit state probabilities,  $P_{gg}$ ,  $P_{ge}$ ,  $P_{eg}$ , and  $P_{ee}$ , where  $P_{ge}$  is the probability of measuring the first qubit in its ground state with the second qubit in its excited state, and so on. We then vary the interaction time  $\tau$ , capturing the evolution of these probabilities. If a resonator has  $n$  photons, the  $n$ th photon will swap between the qubit and resonator at a rate scaling as  $\sqrt{n}$ , while for more complicated states, the interaction is a sum of components oscillating at their respective frequencies, weighted by the photon occupation probabilities [13, 14].

For resonators entangled in a NOON state, a joint measurement should correspond to either  $N$  photons in one resonator and zero in the other, or to the reverse situation; the measurement of the qubits “collapses” the system onto one or the other outcome. Thus in one measurement at most one of the qubits will be in the excited state. When averaged over many measurements, the maximum probability of measuring a particular qubit in  $|e\rangle$  is  $1/2$ , while the probability of measuring both qubits in  $|e\rangle$  should be zero. Therefore we expect that  $P_{eg}$  and  $P_{ge}$  will oscillate between 0 and  $1/2$ ,  $P_{ee}$  will be zero, and  $P_{gg}$  should equal  $1 - P_{ge} - P_{eg} - P_{ee}$ .

Coincidence measurements are shown in Fig. 3 for NOON states up to  $N = 3$ , and are consistent with these expectations. The oscillations seen in these measurements are however insufficient proof of resonator entanglement, as an incoherent mixed state can give the same results. To demonstrate this, we have controllably generated a synthetic ensemble comprising a 50% population of  $|10\rangle$  states and 50%  $|01\rangle$  states [30]. Coincidence

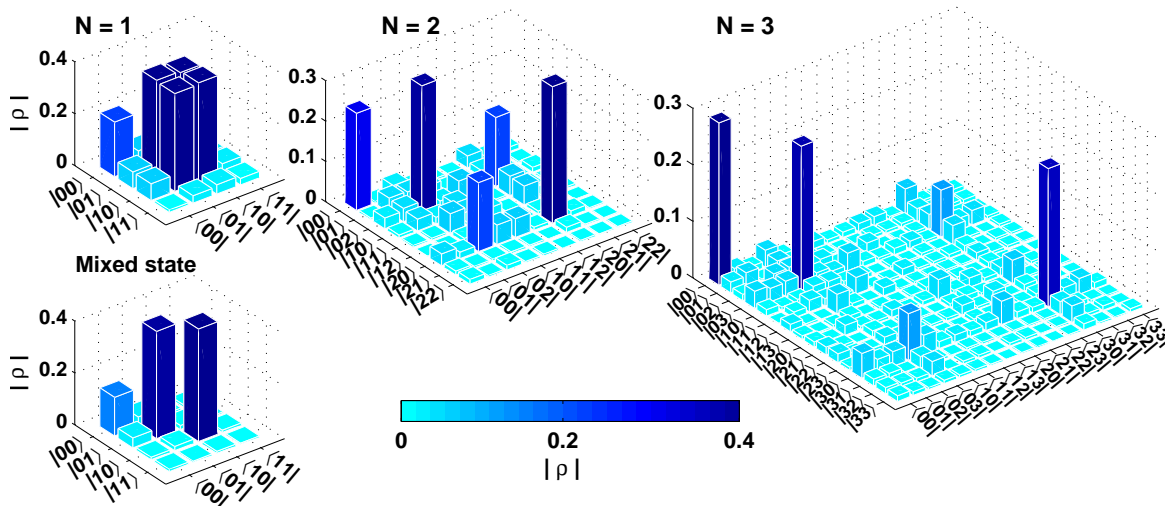


FIG. 4: (Color online) NOON and mixed state density matrix amplitudes, reconstructed in the photon-number basis from bipartite Wigner tomography; states are labeled  $|mn\rangle$  where  $m$  is the photon number in resonator  $A$  and  $n$  that in  $B$ . Bar heights and colors represent matrix element amplitudes. The dominant amplitudes for all three states are in the expected locations, although the off-diagonal elements decrease with  $N$ , due to the finite qubit dephasing time. Errors for the density matrix elements are not shown but are small [30].

measurements (Fig. 3) of this synthetic mixed state generate outcomes identical to those of the  $N = 1$  NOON state.

A more complete resonator measurement, that can resolve entangled from mixed states, uses bipartite Wigner tomography, a nontrivial extension of single resonator tomography [9, 13, 14]. This involves injecting a coherent Gaussian microwave pulse into each of the storage resonators, with controlled amplitude and phase, displacing the resonator states in phase space. The resonators are then simultaneously measured with a joint probability measurement, now as a function of the amplitude and phase of the coherent pulses. From the complete set of measurements, the two-resonator density matrix can be calculated [30].

In Fig. 4 we display the amplitudes of the density matrices measured for resonator NOON states up to  $N = 3$ , as well as for the mixed state. While there are non-idealities, the desired non-zero matrix elements are clearly apparent for the NOON states, while for the mixed state, the density matrix has only zero-valued off-diagonal elements. The state preparation fidelities,  $F = \langle \psi | \rho | \psi \rangle$ , are found to be  $0.76 \pm 0.02$  ( $N = 1$ ),  $0.50 \pm 0.02$  ( $N = 2$ ), and  $0.33 \pm 0.02$  ( $N = 3$ ). For  $N = 1$ , the most probable entanglement of formation [28] is  $EOF = 0.51$ , while for  $N = 2$  and  $N = 3$ ,  $EOF = 0.31$  and  $0.28$ , respectively; for the mixed state, the  $EOF$  is zero. We also calculate the negativity  $N_e(\rho) = \sum_j \max(0, \mu_j)$ , where  $\mu_j$  are the eigenvalues of the partial transpose  $\rho^{\text{PT}}$  of the density matrix [22, 29], and  $N_e(\rho) > 0$  indicates entanglement. The negativities are found to be  $0.56 \pm 0.03$  ( $N = 1$ ),  $0.32 \pm 0.03$  ( $N = 2$ ), and  $0.27 \pm 0.01$  ( $N = 3$ );

for the mixed state we find zero with an upper bound of 0.001. The decrease of these values with photon number  $N$  is compatible with expectations: The state preparation requires phase-coherence of the four-element entangled states for most of the preparation sequence, which is limited by the qubit coherence time  $T_2$  [30]. Other than this technical limitation, the deterministic generation is completely scalable to large  $N$ .

A hallmark of NOON states is their rapid phase evolution [20, 21, 23, 24], which can be verified by Wigner tomography using two distinct methods. For the  $N = 1$  state, after entangling the qubits in a Bell state, we wait for a variable time and then swap the state into the storage resonators. The density matrices measured at three different delay times are shown in Fig. 5(a). The phases of the off-diagonal elements rotate with time due to the qubit-resonator frequency difference, as in Fig. 5(b), showing the expected linear dependence.

This phase-measurement method suffers from the short qubit dephasing time. A second method is to change the phase reference for the coherent pulses used in the Wigner tomography, avoiding storage of the state in the qubit. We add an additional phase to the pulses applied to resonator  $A$  only. The resulting density matrices show the expected rotation of the off-diagonal elements. In Fig. 5(c) we plot the off-diagonal phase angle for different  $N$ ; the  $N = 3$  state evolves three times faster than the  $N = 1$  state, as expected.

We also used tomography to measure the NOON state decay [30]. We find that the off-diagonal elements decrease at approximately the same rate as the diagonal elements, with a decay time  $\tau_D \approx 3 \mu\text{s}$ , consistent with a Markovian environment [14].

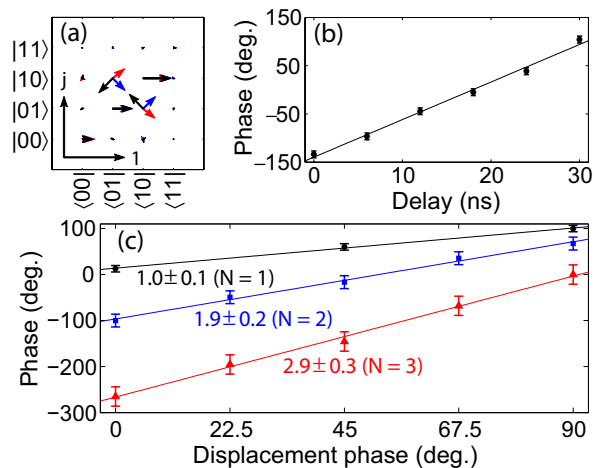


FIG. 5: (Color online) Phase sensitivity of NOON states up to  $N = 3$ . (a) Density matrix for  $N = 1$  NOON state at different times after qubit entanglement. Each element is represented by an arrow, with orientation determined by the phase angle (scale on bottom left). Off-diagonal elements rotate with delay time (black: 0 ns, blue: 12 ns, red: 24 ns), due to frequency difference between the qubit operating point and resonator. Dephasing causes decrease in amplitude of off-diagonal elements. (b) Phase angle of the upper left non-zero off-diagonal element in (a) versus delay time. Line is fit to a rotation rate of  $\Delta f = 21.6 \pm 0.8$  MHz, which corresponds well to set frequency difference. Error bars indicate maximum phase uncertainty. (c) Rotation angle of off-diagonal element versus controlled, additional phase angle used in coherent state displacement. Lines are fits (slopes indicated on plot), consistent with expected phase sensitivity. Confidence bounds are as in (b), with uncertainty increasing with  $N$  due to increased phase sensitivity.

We note that the generation sequence allows an additional flexibility: We can add different numbers of quanta to the resonators, thus generating MOON states,  $|\psi\rangle = |M0\rangle + |0N\rangle$ . An example with  $M = 2$  and  $N = 1$  is detailed in [30].

The capabilities we have demonstrated here, generating complex entangled photon states in two resonators, hold promise for new quantum architectures in which superconducting resonators play a more central role. The protocol can be extended in a natural way to entangle larger numbers of resonators, allowing, e.g., the direct generation of resonator GHZ and W states [2, 4, 9, 16, 21, 23]. The longer coherence times achievable in superconducting resonators will be of direct utility in performing more complex quantum algorithms, furthering the capabilities of superconducting quantum circuit architectures.

**Acknowledgments.** We thank K. Audenaert for assistance in entanglement-of-formation calculations. This work was supported by IARPA under ARO award W911NF-04-1-0204. M.M. acknowledges support from an Elings Postdoctoral Fellowship. H.W. acknowledges

partial support by the Fundamental Research Funds for the Central Universities in China (Program No. 1A3000\*172210301[26]). Devices were made at the UC Santa Barbara Nanofabrication Facility, a part of the NSF-funded National Nanotechnology Infrastructure Network.

\* To whom correspondence should be addressed. E-mail: anc@physics.ucsb.edu

- [1] S. Haroche and J. M. Raimond, *Exploring the Quantum - Atoms, Cavities and Photons* (Oxford University Press, Oxford UK, 2006).
- [2] R. Blatt and D. Wineland, *Nature (London)* **453**, 1008 (2008).
- [3] R. Hanson, L. P. Kouwenhoven, J. R. Petta, S. Tarucha, and L. M. K. Vandersypen, *Rev. Mod. Phys.* **79**, 1217 (2007).
- [4] P. Neumann *et al.*, *Science* **320**, 1326 (2008).
- [5] J. Clarke and F. K. Wilhelm, *Nature (London)* **453**, 1031 (2008).
- [6] M. Neeley *et al.*, *Nature (London)* **467**, 570 (2010).
- [7] L. DiCarlo *et al.*, *Nature (London)* **467**, 574 (2010).
- [8] H. Mabuchi and A. C. Doherty, *Science* **298**, 1372 (2002).
- [9] D. Leibfried, R. Blatt, C. Monroe, and D. J. Wineland, *Rev. Mod. Phys.* **75**, 281 (2003).
- [10] J. D. Jost *et al.*, *Nature (London)* **459**, 683 (2009).
- [11] R. J. Schoelkopf and S. M. Girvin, *Nature (London)* **451**, 664 (2008).
- [12] M. Hofheinz *et al.*, *Nature (London)* **454**, 310 (2008).
- [13] M. Hofheinz *et al.*, *Nature (London)* **459**, 546 (2009).
- [14] H. Wang *et al.*, *Phys. Rev. Lett.* **103**, 200404 (2009).
- [15] A. Rauschenbeutel *et al.*, *Phys. Rev. A* **64**, 050301 (2001).
- [16] S. B. Papp *et al.*, *Science* **324**, 764 (2009).
- [17] M. Mariani *et al.*, *Phys. Rev. B* **78**, 104508 (2008).
- [18] S. T. Merkel and F. W. Wilhelm, *New J. Phys.* **12**, 093036 (2010).
- [19] F. W. Strauch, K. Jacobs, and R. W. Simmonds, *Phys. Rev. Lett.* **105**, 050501 (2010).
- [20] A. N. Boto *et al.*, *Phys. Rev. Lett.* **85**, 2733 (2000).
- [21] T. Nagata *et al.*, *Science* **316**, 726 (2007).
- [22] L. K. Shalm, R. B. A. Adamson, and A. M. Steinberg, *Nature (London)* **457**, 67 (2009).
- [23] J. A. Jones *et al.*, *Science* **324**, 1166 (2009).
- [24] I. Afek, O. Ambar, and Y. Silberberg, *Science* **328**, 879 (2010).
- [25] J. M. Martinis, *Quantum Information Processing* **8**, 81 (2009).
- [26] J. Q. You, Y.-X. Liu, C. P. Sun, and F. Nori, *Phys. Rev. B* **75**, 104516 (2007).
- [27] M. Neeley *et al.*, *Science* **325**, 722 (2009).
- [28] K. Audenaert, F. Verstraete, and B. DeMoor, *Phys. Rev. A* **64**, 052304 (2001).
- [29] A. Peres, *Phys. Rev. Lett.* **77**, 1413 (1996).
- [30] See supplementary below for additional discussion and analysis.

**Supplementary Material for  
“Deterministic entanglement of photons in two  
superconducting microwave resonators”**

**MATERIALS AND METHODS**

The device fabrication is similar to that published previously [S1]. The half-wavelength superconducting coplanar waveguide resonators are made of rhenium deposited on a *c*-axis single-crystal sapphire substrate, with a 5  $\mu\text{m}$ -wide center signal trace and 10  $\mu\text{m}$  gaps to the ground plane metallization on either side of the center trace. We place a single lithographed shorting strap connecting the two ground planes at the midpoint of each resonator to improve the quality of the grounding. This point is a voltage node for the fundamental half-wave resonant mode, so that there is minimal additional dielectric loss from the shorting strap’s underlying amorphous Si insulating film [S2].

In the circuit layout, the coupling resonator *C* is designed to have a higher resonance frequency than the two state storage resonators *A* and *B*. This prevents the qubit frequencies from having to cross the *C* resonator frequency during NOON state amplification. The two storage resonators *A* and *B* are designed with slightly different resonance frequencies, to avoid possible interference between the resonators. The full frequency span in the design was chosen to be about 550 MHz, within the dynamic range of our custom microwave electronics. The two superconducting phase qubits and coplanar waveguide resonators are fabricated together, using our standard multi-layer process [S3]. We use interdigitated coupling capacitors between the qubits and the resonators, calculated to each have a coupling capacitance of 1.9 fF. The actual coupling strengths vary slightly with resonator frequency; the detailed component parameters are listed in Table S1.

**GENERATION SEQUENCE TUNE-UP**

The time required for each qubit-resonator *i*-SWAP is calibrated separately. The swap times obtained from these calibrations scale correctly as  $\sqrt{n}$  with the number of photons *n* in the resonator [S5] and also depend on the state of the qubit. Examples of the swap calibrations for a one-photon swap between qubit  $q_0$  and resonator *A* are shown in Fig. S1, for both the  $|g\rangle \leftrightarrow |e\rangle$  and  $|e\rangle \leftrightarrow |f\rangle$  transitions. The swap time for the  $|e\rangle \leftrightarrow |f\rangle$  transition is approximately  $1/\sqrt{2}$  times that for the  $|g\rangle \leftrightarrow |e\rangle$  transition. This scaling is as expected, as the multi-level phase qubit can be well-approximated as a weakly nonlinear harmonic oscillator for the energy levels confined by the qubit’s metastable potential well. The scaling confirms that we can use harmonic-oscillator-like raising and low-

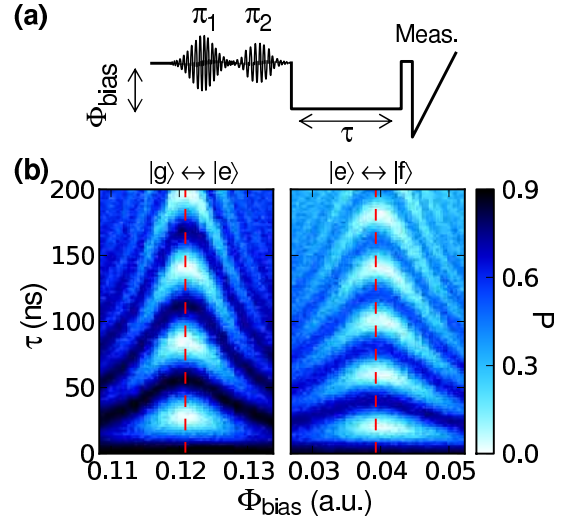


FIG. S1: (Color online) One-photon swaps between qubit  $q_0$  and resonator *A*. (a) Pulse sequence for measuring swaps between the qubit  $|e\rangle \leftrightarrow |f\rangle$  transition and resonator *A*. When off-resonance, the qubit is excited by a pair of  $\pi$  pulses, with the first pulse  $\pi_1$  taking the qubit from  $|g\rangle$  to  $|e\rangle$  and the second pulse  $\pi_2$  making the transition from  $|e\rangle$  to  $|f\rangle$ . The qubit  $|e\rangle \leftrightarrow |f\rangle$  transition is then tuned close to resonance with resonator *A* and the qubit and resonator left to interact for a time  $\tau$ . The triangular pulse at the end is used to measure the probability of the qubit being in the  $|f\rangle$  state at the end of the sequence. (b) Left: Qubit  $|g\rangle \leftrightarrow |e\rangle$  swaps with resonator *A*. The qubit is prepared as in (a), but without the second pulse  $\pi_2$ . The qubit  $|e\rangle$  probability (color bar) is plotted as a function of interaction time  $\tau$  and frequency tuning  $\Phi_{\text{bias}}$ . Oscillations in probability are due to the qubit excitation swapping with the resonator. Right: Qubit  $|e\rangle \leftrightarrow |f\rangle$  swaps with resonator *A*; the preparation of the qubit is as in (a) and the plot shows the  $|f\rangle$ -state probability as a function of interaction time  $\tau$  and qubit flux bias  $\Phi_{\text{bias}}$ . Red dashed lines indicate the on-resonance  $\Phi_{\text{bias}}$  values used in the experiment. The swap frequency for the on-resonance  $|e\rangle \leftrightarrow |f\rangle$  transition is  $1.403 \approx \sqrt{2}$  times that for the on-resonance  $|g\rangle \leftrightarrow |e\rangle$  transition.

ering operators for the three-level qubit, as was done in the numerical simulations (see below).

Figure S2 shows the detailed pulse sequence used to generate and measure the  $N = 2$  NOON state. Sequence steps in general are calibrated and checked separately to maximize preparation fidelity, when possible. For example, we first optimize the qubit Bell state preparation at the end of step I in the preparation sequence detailed in Fig. S2. The fidelity for the Bell state is above 0.80, with entanglement of formation 0.59, which agrees well with numerical simulations, performed using a pure dephasing time  $T_\phi = 300$  ns for the qubits (see below). State tomography of the qubits is also as expected: Fig. S2(b) shows the density matrices extracted from coupled qubit tomography, measured at different times during the  $N = 2$  NOON state preparation. We note that at the end of the sequence, both qubits should return to their ground

circuit component	$f_r$ (GHz)	$f_{ g\rangle\leftrightarrow e\rangle}$ (GHz)	$f_{\text{nonlinear}}$ (GHz)	$T_1$ (ns)	$T_\phi$ (ns)
A	6.340	-	-	3500	$\gg T_1$
B	6.286	-	-	3300	$\gg T_1$
C	6.816	-	-	3400	$\gg T_1$
$q_0$	-	$\sim 6.65$	$\approx 0.20$	450	200 – 300
$q_1$	-	$\sim 6.58$ or $6.68$	$\approx 0.20$	320	200 – 300
Coupling strength $g/\pi$ (MHz)		$q_0 \leftrightarrow A$	$q_0 \leftrightarrow C$	$q_1 \leftrightarrow B$	$q_1 \leftrightarrow C$
		17.8	20.0	17.4	20.0

TABLE S1: Resonator and qubit parameters. The qubit parameters are quoted for when the qubits are off-resonance (see below). The qubit nonlinearity  $f_{\text{nonlinear}}$  is the frequency difference between the  $|g\rangle \leftrightarrow |e\rangle$  and  $|e\rangle \leftrightarrow |f\rangle$  transitions. The phase coherence time  $T_\phi$  is obtained using a Ramsey interference experiment, which yields the Ramsey time  $T_2$ , from which we calculate  $1/T_\phi = 1/T_2 - 1/(2T_1)$ .  $T_\phi$  measured for resonators similar to those used here [S4] satisfies  $T_\phi \gg T_1$ ; we assume the same applies here.  $T_\phi$  for the qubits decreases with increasing length of the pulse sequence due to the  $1/f$  nature of the phase noise. For most state generation sequences used in this experiment, of typical length 50 to 100 ns, the qubit  $T_\phi$  is in the range of 200 to 300 ns. Coupling strengths correspond to the measured splitting in frequency units, with  $g$  appearing in the Hamiltonian shown in Eq. (S1).

states. Experimentally we observe small populations in the excited states  $|e\rangle$  due to decoherence and pulse imperfections. The exact qubit state after the NOON state generation is measured and is used as the initial state for the qubits when performing Wigner tomography on the storage resonators (see below).

## NUMERICAL SIMULATIONS

Numerical simulations were performed using the model Hamiltonian

$$\begin{aligned}
H = & \sum_{q_i=q_0,q_1} H_{q_i} + \sum_{j=A,B,C} \hbar\omega_j \left( b_j^\dagger b_j + \frac{1}{2} \right) \\
& + \sum_{(q_i,j)} \hbar g_{q_i \leftrightarrow j} (a_{q_i}^\dagger b_j + a_{q_i} b_j^\dagger) \\
& + \sum_{q_i=q_0,q_1} \frac{1}{2} \hbar [\Omega_{q_i}(t) a_{q_i}^\dagger + \Omega_{q_i}^*(t) a_{q_i}], \quad (\text{S1})
\end{aligned}$$

where  $H_{q_i}$  is the Hamiltonian of the qubit  $q_i$ ,  $a_{q_i}^\dagger$  and  $a_{q_i}$  ( $b_j^\dagger$  and  $b_j$ ) are the raising and lowering operators for the 3-level qubit  $q_i$  (resonator  $j$ ),  $g_{q_i \leftrightarrow j}$  is the coupling strength between qubit  $q_i$  and resonator  $j$ , with a sum over all possible qubit-resonator combinations, such that  $(q_i, j) \in \{(q_0, A), (q_0, C), (q_1, B), (q_1, C)\}$  and  $\Omega_{q_i}(t)$  is the time-dependent, two-tone ( $f_{|g\rangle\leftrightarrow|e\rangle}$  and  $f_{|e\rangle\leftrightarrow|f\rangle}$ ) microwave drive on qubit  $q_i$ .

The 3-level qubit Hamiltonian  $H_{q_i}$  was approximated as

$$H_{q_i} = \begin{bmatrix} 0 & 0 & 0 \\ 0 & \hbar f_{|g\rangle\leftrightarrow|e\rangle} & 0 \\ 0 & 0 & \hbar f_{|g\rangle\leftrightarrow|f\rangle} \end{bmatrix}_{q_i}, \quad (\text{S2})$$

where for simplicity we assumed a constant nonlinearity  $f_{|g\rangle\leftrightarrow|e\rangle} - f_{|e\rangle\leftrightarrow|f\rangle} = 200$  MHz, so that  $f_{|g\rangle\leftrightarrow|f\rangle} \simeq 2f_{|g\rangle\leftrightarrow|e\rangle} - 200$  MHz. We approximated the multi-level qubit  $a_{q_i}^\dagger$  and  $a_{q_i}$  by the raising and lower operators for the lowest three levels of a harmonic oscillator, as discussed above.

Decoherence was approximated using the Lindblad master equation taking into account the Markovian environment [S6], where two characteristic decay times, the energy relaxation time  $T_1$  and the pure dephasing time  $T_\phi$ , were used for each resonator and qubit.

The simulations do not directly account for the non-Markovian  $1/f$  character of the phase noise in the qubits. To account for this, we used a sequence-time dependent  $T_\phi$  for each qubit, as obtained from Ramsey interference measurements. We used  $T_\phi = 300$  ns for  $\sim 50$  ns-long sequences and  $T_\phi = 200$  ns for  $\sim 100$  ns-long sequences. The resulting simulations agree reasonably well with the experimental measurements.

## BIPARTITE WIGNER TOMOGRAPHY

### Displacement Pulses

The bipartite Wigner tomography is an extension of a method described elsewhere [S7, S5, S4]. We displace each resonator with Gaussian pulses  $|\alpha\rangle$  and  $|\beta\rangle$  (resonator  $A$  and  $B$ , respectively), with variable phase and amplitude. The values of  $\alpha$  and  $\beta$  are distributed over several concentric circles in the complex plane, centered on the origin, where the distribution of values varies approximately with the size  $N$  of the NOON state. The radii of the circles run through the set  $r_j \in \{0, 0.2, 0.7, 0.9, 1.3\}$ , in square-root of photon number units [S5]. The pulse values are evenly distributed on

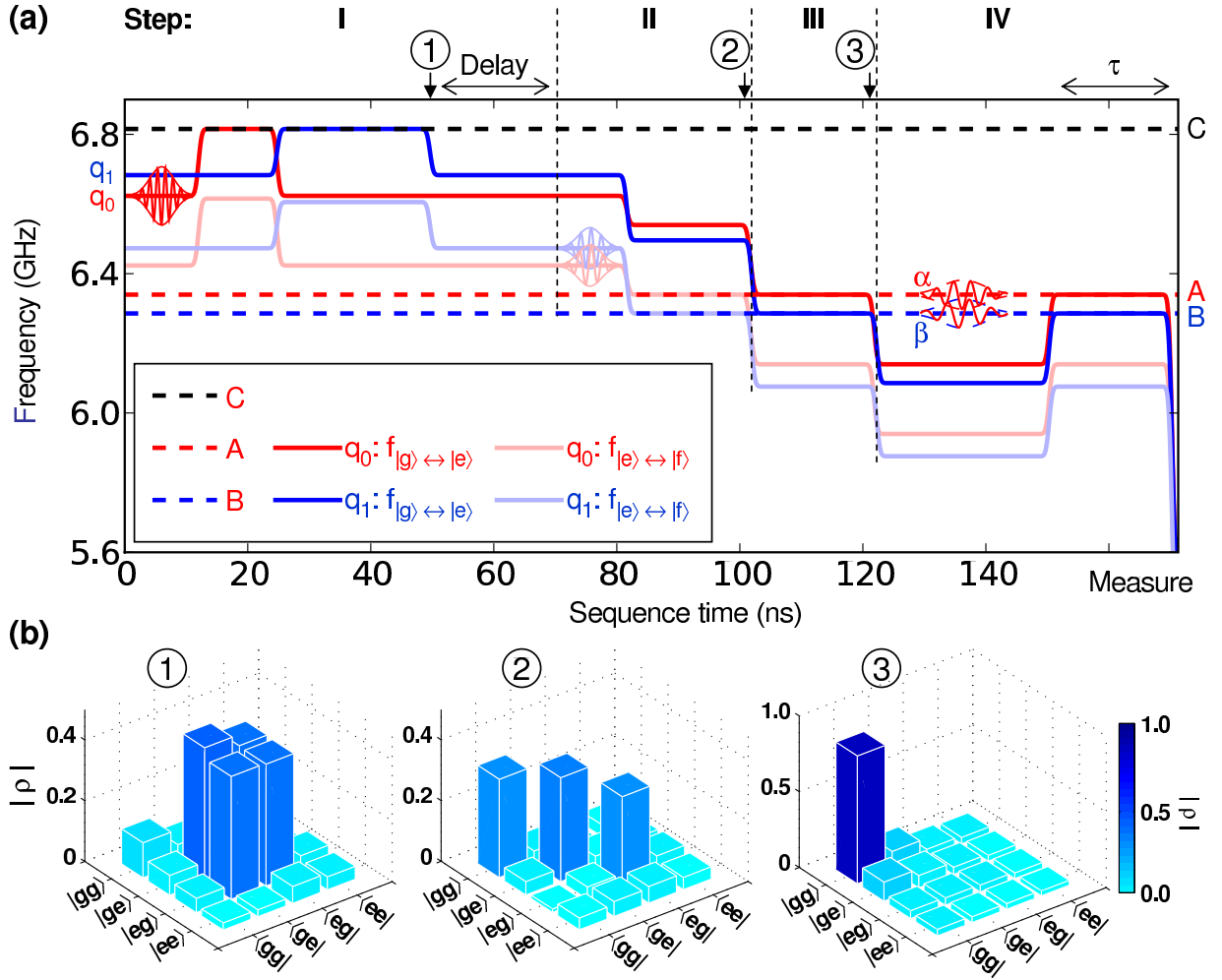


FIG. S2: (Color online) NOON state preparation. (a) Sequence to generate and measure  $N = 2$  NOON state. Qubit transition frequencies  $|g\rangle \leftrightarrow |e\rangle$  (dark-color solid lines) and  $|e\rangle \leftrightarrow |f\rangle$  (light solid lines) are tuned to control coupling of each qubit to resonators (dashed lines);  $q_0$  in red,  $q_1$  in blue. Vertical lines divide sequence into steps; circled numbers indicate points where qubit tomography was performed. Step I: A  $\pi_{|g\rangle \rightarrow |e\rangle}$  pulse excites  $q_0$  to  $|e\rangle$ , followed by a  $\sqrt{i}$ -SWAP entangling  $q_0$  and resonator  $C$ . A full  $i$ -SWAP between  $C$  and  $q_1$  disentangles the resonator and generates the qubit Bell state  $|eg\rangle + |ge\rangle$ . For the  $N = 1$  NOON state this entanglement is transferred to the storage resonators (not shown). For  $N > 1$ ,  $\pi_{|e\rangle \rightarrow |f\rangle}$  pulses excite each qubit to yield  $|fg\rangle + |gf\rangle$ . Both qubits'  $|e\rangle \leftrightarrow |f\rangle$  transitions are then tuned to the respective storage resonators, and an  $i$ -SWAP transfers one photon to the resonators. For  $N = 3$ , this is repeated to transfer a second photon (not shown). In step III, both qubits'  $|g\rangle \leftrightarrow |e\rangle$  transitions are tuned to the resonators and an  $i$ -SWAP transfers the remaining excitation to the resonators, completing the generation, leaving both qubits in their ground states. Step IV: State analysis. The storage resonator  $A$  ( $B$ ) is displaced in phase space by a Gaussian pulse  $|\alpha\rangle$  ( $|\beta\rangle$ ), followed by an on-resonance interaction with each qubit's  $|g\rangle \leftrightarrow |e\rangle$  transition for a time  $\tau$ , followed by joint-qubit state readout. Many repetitions of this sequence are combined to generate joint-qubit state probabilities  $P_{gg}$ ,  $P_{ge}$ ,  $P_{eg}$ , and  $P_{ee}$  versus  $\tau$ . The joint-qubit state probabilities can be used to obtain the two-resonator density matrix (see text). (b) Qubit density matrices extracted from tomography at circled points in (a). (1) Qubit Bell state. (2) Qubit state after transferring first photon into resonators. This is a state with qubits and resonators entangled, so the density matrix is as expected. (3) Qubit state after  $N = 2$  NOON state generation. Both qubits are very nearly in their ground states, and thus can be used to measure the resonators.

each circle, with complex values  $r_j \exp(i2\pi\ell/N_{r_j})$ , where  $\ell$  ranges from 1 to  $N_{r_j}$  and  $N_{r_j}$  is an integer ranging from 1 ( $r_j = 0$ ), 5 or 6 ( $r_j = 0.2$ ), up to 9 to 15 ( $r_j = 1.3$ ), depending on the number of photons in the NOON state.

We use every possible combination of values of  $\alpha$  and  $\beta$  distributed over the circles of the same radius for tomography, i.e., for each value of  $\alpha$ , we use all  $\beta$  values with the

same amplitude as  $\alpha$ . The total number of displacement pulse combinations is thus quite large and increases with the photon number  $N$  in the NOON state, typically involving of order a few hundred pulses. The displacement

pulses can be expressed as

$$\begin{aligned} D_{AB}(\alpha_j, \beta_k) &= D_A(\alpha_j) \otimes D_B(\beta_k) \\ &= e^{\alpha_j b_A^\dagger - \alpha_j^* b_A} \otimes e^{\beta_k b_B^\dagger - \beta_k^* b_B}. \end{aligned} \quad (\text{S3})$$

### Photon Populations

For an initial joint-resonator density matrix  $\rho_{\text{initial}}$ , the displacement pulses shift the density matrix to

$$\rho = D_{AB}(-\alpha_j, -\beta_k) \rho_{\text{initial}} D_{AB}(\alpha_j, \beta_k). \quad (\text{S4})$$

By bringing both qubits (initially in their  $|g\rangle$  states) on resonance with the resonators, the joint number states contained in two resonators, i.e., the diagonal elements of  $\rho$ , can be read out, as each diagonal element swaps with the qubits at a different rate [S5], resulting in a distinct time-dependence for the probabilities  $P_{gg}$ ,  $P_{ge}$ ,  $P_{eg}$ , and  $P_{ee}$ . These can be numerically simulated using the device parameters from Table S1.

As displayed in Fig. S2(b), there is a small non-zero occupation of the excited state of each qubit after the state generation sequence, due to decoherence and pulse imperfections. We use the measured qubit state after the state generation sequence as the qubit initial condition when numerically simulating the tomography. Using these simulations, we obtain the time dependence for each of the probabilities  $P_{gg}$ ,  $P_{ge}$ ,  $P_{eg}$ , and  $P_{ee}$  corresponding to different combinations of photon number (Fock) states in the two storage resonators. Examples of these probability traces are shown in Fig. S3(a) for some selected initial states. The time-dependent traces for these probabilities, for the set of Fock states  $\{|m\rangle_A |n\rangle_B, m = 0, 1, 2, \dots, n = 0, 1, 2, \dots\}$ , are then used to decompose the experimentally-measured time traces, which yields the probability distribution for the Fock number states contained in the storage resonators. This thus yields the diagonal elements of the experimentally-measured displaced density matrix  $\rho$ .

We obtain the diagonal elements of  $\rho$  by doing a least-squares fit of the time-dependent probabilities, corrected for measurement fidelity. We use the MATLAB packages YALMIP and SeDuMi for the fitting. The number of fitting parameters is the number of diagonal elements, directly determined by the maximum photon number state contained in the resonators, plus the number of photon quanta added by the displacement pulses  $|\alpha\rangle$  and  $|\beta\rangle$ . Fits are done with constraints  $P_{mn} \geq 0$  and  $\sum_{m,n} P_{mn} = 1$  to return meaningful probability values. Examples of these fits are shown in Fig. S3, for the  $N = 1$  NOON state.

Delay (ns)	$\langle 01 \rho 01\rangle$	$\langle 10 \rho 10\rangle$	$\langle 01 \rho 10\rangle$	$\Delta \langle 01 \rho 10\rangle $
16	0.36(1)	0.386(9)	0.328-0.037i	0.009
250	0.31(1)	0.32(1)	0.31+0.01i	0.01
500	0.32(1)	0.31(1)	0.285-0.068i	0.009
750	0.27(1)	0.27(1)	0.259+0.017i	0.008
1000	0.27(1)	0.28(1)	0.261+0.010i	0.008
1250	0.23(1)	0.24(1)	0.215-0.037i	0.008
1500	0.24(1)	0.23(1)	0.229-0.033i	0.008
2000	0.20(1)	0.20(1)	0.198+0.001i	0.006
2500	0.17(1)	0.17(2)	0.155-0.005i	0.008
3000	0.14(2)	0.15(2)	0.13+0.04i	0.01
4000	0.08(2)	0.09(4)	0.06+0.03i	0.01

TABLE S2: Density matrix elements as a function of delay time for the  $N = 1$  NOON state shown in Fig. S4. Uncertainties for the diagonal elements are in parentheses, while the magnitude of the uncertainty for the off-diagonal terms are given in the last column.

### Joint-Resonator Density Matrices

With the diagonal elements of  $\rho$  measured for a set of displacements  $\{D_{AB}(\alpha_j, \beta_k)\}$ ,  $\rho_{\text{initial}}$  can be solved for by inverting Eq. (S4) through a linear least-squares fit, while restricting the density matrix to be Hermitian. The resulting density matrices may have small negative eigenvalues due to noise. We use the MATLAB packages YALMIP and SeDuMi to perform semi-definite convex optimization programming, allowing us to find a physical density matrix that is closest to the actual matrix.

When solving for  $\rho_{\text{initial}}$  of a NOON state, we restrict the dimension of  $\rho_{\text{initial}}$  to an  $N \times N$  matrix, even though the dimension of  $\rho$  can be significantly larger than this due to the displacement pulses. We zero-pad the elements in  $\rho_{\text{initial}}$  that have photon indices larger than  $N$ . This approach is validated by the coincidence measurements (see main text), as we do not detect any frequency components for number states above  $N$  prior to injecting a displacement pulse.

### NOON STATE DECAY DYNAMICS

The Wigner tomography allows us to study the decoherence dynamics of the bipartite system [S4]. The experimental results, compared with numerical simulations, are shown in Fig. S4, with relevant elements in Table S2. We note that the time evolution of the off-diagonal elements in the two-resonator density matrix, which represent inter-resonator coherence, is different from the evolution of the corresponding off-diagonal elements for a single resonator, which represent intra-resonator coherence [S4].

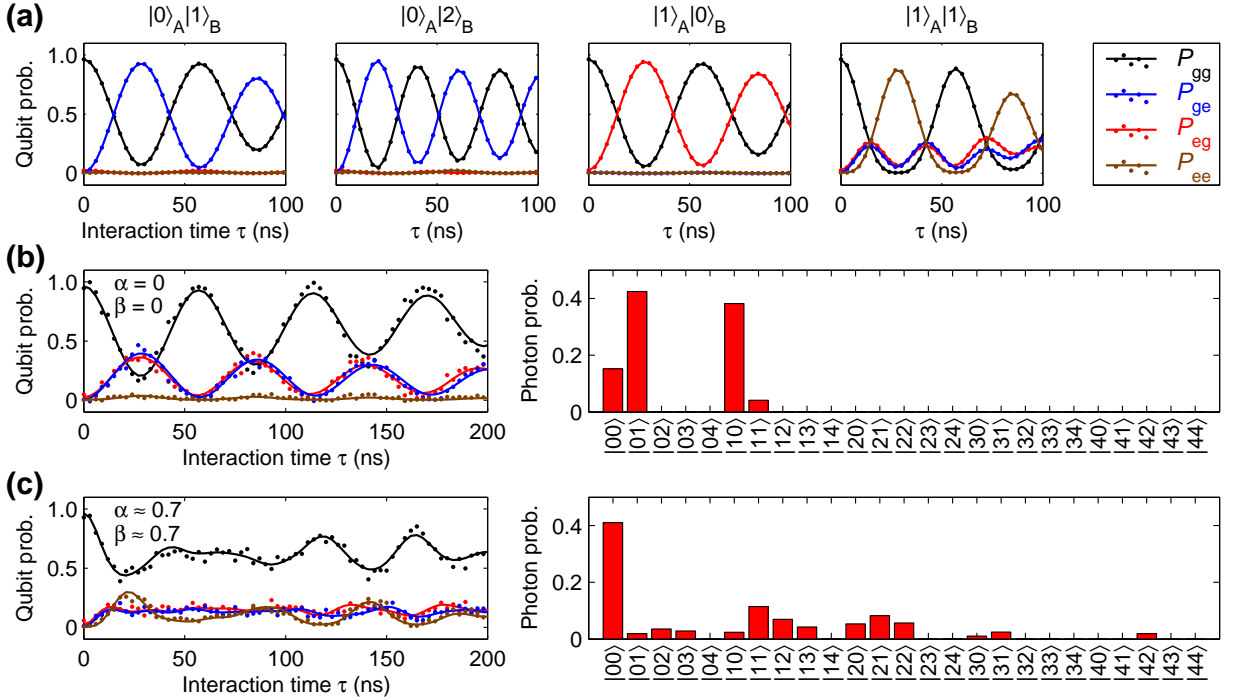


FIG. S3: (Color online) Joint-state probabilities and photon number distribution analysis for  $N = 1$  NOON state. (a) Joint-qubit state probabilities from numerical simulations, for a few selected initial resonator states in  $A$  and  $B$ , as indicated. Lines are a guide to the eye. Device parameters are as in Table S1. (b) Left panel, measured joint-qubit state probabilities for null displacement pulses  $\alpha, \beta = 0$ . Lines are fits to the data. The fit joint-photon probability distributions  $\rho_{|m\rangle_A|n\rangle_B}$  are displayed in the right panel. The most significant occupations are in  $|0\rangle_A|1\rangle_B$  and  $|1\rangle_A|0\rangle_B$ , as expected for this state. (c) Left panel, measured joint-qubit state probabilities for the displaced state with  $\alpha = 0.7$  and  $\beta = 0.7$  (square-root of photon number units). Lines are fits to the data. The fit joint-photon probability distributions  $\rho_{|m\rangle_A|n\rangle_B}$ , shown in the right panel, are significantly different from those shown in (b) due to the displacement. The matrix elements for the higher photon number states are omitted for viewing, although these may not be negligible for larger displacement pulses.

### Error Analysis

Statistical errors in the qubit probability measurements as well as uncertainty in the amplitude calibration for the displacement pulses  $\alpha_j$  and  $\beta_k$  are used to estimate the uncertainty in the amplitude and phase of each density matrix element. These errors are found to be small, in part because the constraints on the analysis filters unrealistic values. Instead we find that slow phase drifts in the electronics, perhaps dominated by ambient temperature fluctuations, give the main phase uncertainties, especially during long measurements. Evaluating a single density matrix usually takes a relatively short time during which these drifts are minimal. However, measuring a series of density matrices such as Fig. 5 in the main paper, takes a much longer time, typically 12 to 20 hours, allowing for more significant drifts. These mostly affect the phases of the density matrix elements, rather than the amplitudes.

### Validation

The bipartite Wigner tomography was validated by several consistency checks. (1) The density matrix is as expected for a range of different states, including the highly entangled NOON states, the energy eigenstates  $|2\rangle_A|0\rangle_B$  (Fig. S5(a)), the separable (product) state  $(|0\rangle - |1\rangle)_A(|0\rangle - |1\rangle)_B$  (Fig. S5(b)) and the unentangled mixed states (see below). (2) The NOON states display the expected phase sensitivity as a function of photon number  $N$ , as shown in Fig. 5 in the main paper and Table S3. (3) The NOON state fidelity and entanglement of formation agree reasonably well with numerical simulations. (4) The time-dependence of the density matrix elements, showing uniform exponential decay of all elements, is as expected and agrees with numerical simulations, as shown in Fig. S4 and Table S2. (5) The calculated negativities are significantly above zero for the NOON states and precisely zero (within the measurement error) for the unentangled mixed state (see below).

We note that bipartite Wigner tomography can measure any matrix element with a relatively high accuracy, as we can displace the system by an arbitrary amount

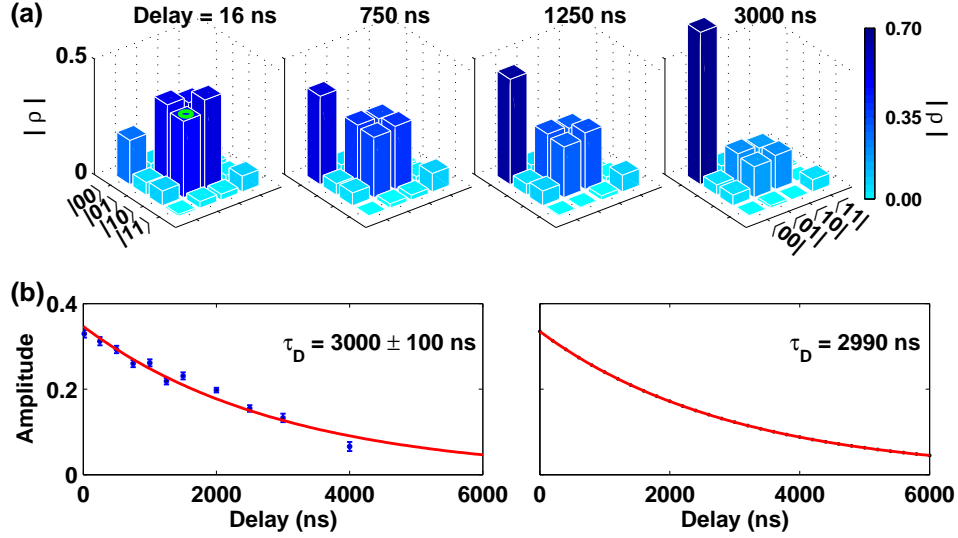


FIG. S4: (Color online) Decay of the  $N = 1$  NOON state. (a) Density matrix amplitudes for the  $N = 1$  NOON state at selected delay times. Bar heights and colors represent the matrix element amplitude, scale on right. The off-diagonal element amplitudes decrease at a rate close to that of the diagonal counterparts. Values for the relevant elements are tabulated in Table S2. (b) Left: Experimental data, showing amplitude of the off-diagonal element as marked by a green ellipse in the first panel in (a), plotted versus post-preparation time. Line is a fit yielding a single decay time  $\tau_D$ , consistent with a Markovian dissipative environment [S8]. Right: Numerical simulation of the same density matrix element as the experiment, with the line an exponential fit. The simulation uses the measured density matrix as the initial condition and the resonator  $T_1$  value listed in Table S1. The simulated decay time  $\tau_D$  is in good agreement with experiment.

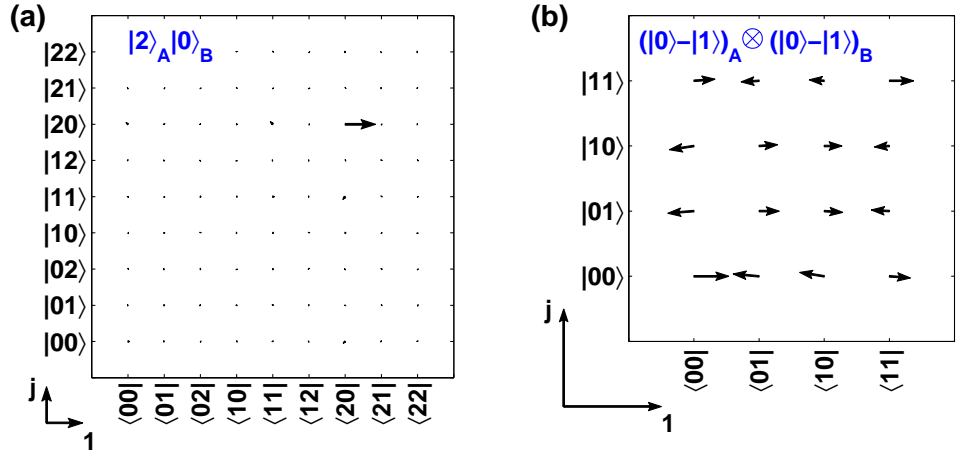


FIG. S5: (Color online) Benchmark resonator states used to validate the bipartite Wigner tomography. (a) Photon-number representation of the two-resonator density matrix (error bars not shown), for the energy eigenstate  $|2\rangle_A|0\rangle_B$ , generated by pumping two photons into resonator  $A$  while leaving  $B$  in its ground state. The magnitude of each matrix element is represented by the full length of the corresponding arrow and the phase angle determined by the direction of the arrow in the complex plane (scale on bottom left). Density matrix is as expected from state preparation. (b) Two-resonator density matrix (error bars not shown) for the test resonator state  $(|0\rangle - |1\rangle)_A(|0\rangle - |1\rangle)_B$ , generated by creating the  $|g\rangle - i|e\rangle$  state in each qubit, followed by a complete  $i$ -SWAP transfer to each storage resonator. Non-idealities are likely due to inaccuracies in the preparation pulses.

in phase space. Even for relatively small off-diagonal elements, such as the desired off-diagonal term in the  $N = 3$  NOON state, the tomography can unambiguously evaluate this element and measure its sensitivity to external phase perturbations.

### Ensemble of Mixed States

We use a synthetic ensemble of mixed states to illustrate the hazards involved in relying purely on coincidence measurements for demonstrating NOON-state entanglement. The ensemble comprises a mixture of 50%  $|1\rangle_A|0\rangle_B$  and 50%  $|0\rangle_A|1\rangle_B$  states, i.e., an ensemble with

	color	$\langle 01 \rho 01\rangle$	$\langle 10 \rho 10\rangle$	$\langle 01 \rho 10\rangle$
Fig. 5(a)	black	0.327	0.460	-0.229+0.239i
	blue	0.318	0.464	0.204+0.200i
	red	0.301	0.439	0.196-0.156i

TABLE S3: (Color online) Density matrix elements for the data shown in Figs. 5(a) of the main paper, coded by color (uncertainties not shown). The phase uncertainty in the off-diagonal elements is dominated by the slow phase drift of our electronics (see text).

the same probability of being measured in either of the states forming the  $N = 1$  NOON state, but without any entanglement. This is done by generating the pure state  $|1\rangle_A|0\rangle_B$  and measuring the time-dependent joint probabilities  $P_{gg}(\tau)$ ,  $P_{ge}(\tau)$ ,  $P_{eg}(\tau)$ , and  $P_{ee}(\tau)$  for this state. We then generate the other component of the ensemble, the pure state  $|0\rangle_A|1\rangle_B$ , and repeat the generation and measurement procedure. Each value of  $\tau$  involves 300 repeats of the preparation and measurement sequence for each of the pure states. We then combine the measurement results with equal weights, creating the joint probabilities for the synthetic ensemble; these data are shown in the main paper. The tomographic analysis yielding the density matrices is done in the usual way. The outcome of the ensemble measurements are shown in the main text, with the joint probabilities evolving in a way indistinguishable from the entangled NOON states, but the density matrix for the ensemble revealing a complete lack of entanglement, as witnessed by the negligible values for the off-diagonal elements.

### MOON STATE

The NOON-state generation protocol can be simply generalized to generate MOON states, with different photon numbers in the two entangled resonators. The generation is similar to the NOON state sequence shown in Fig. S2. We assume  $M > N$ : After generating the Bell entanglement between two qubits at the end of step I (Fig. S2(a)), we repeat step II  $N - 1$  times, yielding the four-fold entangled state  $|eg(N - 1)0\rangle + |ge0(N - 1)\rangle$ . The photon amplification and transfer process (step II) is then applied  $M - N$  times, but only to qubit  $q_0$  and resonator

$A$ , yielding the state  $|eg(M - 1)0\rangle + |ge0(N - 1)\rangle$ . The final qubit excitations are then transferred in step III, resulting in the MOON state  $|gg\rangle \otimes (|M0\rangle + |0N\rangle)$ , with the qubits disentangled from the resonators. A MOON state generated in this fashion, with  $M = 2$  and  $N = 1$ , is shown in Fig. S6.

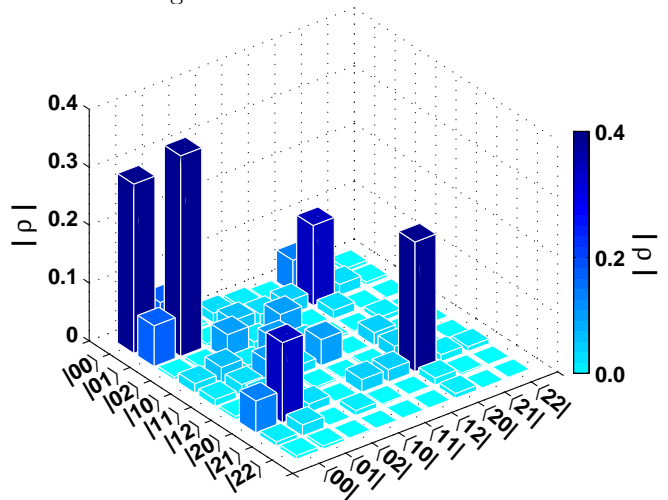


FIG. S6: (Color online) Measured density matrix (errors not shown) of the MOON state with  $M = 2$  and  $N = 1$ . The generation sequence is as described in the text. The state fidelity is  $0.42 \pm 0.01$ , lower than our typical NOON state fidelity, due to technical issues with the particular device used for this experiment; the entanglement of formation is 0.16. The negativity is  $N_e = 0.14 \pm 0.01$ , indicating a statistically significant entanglement.

\* To whom correspondence should be addressed. E-mail: anc@physics.ucsb.edu

- [S1] H. Wang *et al.*, *Phys. Rev. Lett.* **101**, 240401 (2008).
- [S2] A. D. O'Connell *et al.*, *Appl. Phys. Lett.* **92**, 112903 (2008).
- [S3] J. M. Martinis, *Quantum Information Processing* **8**, 81 (2009).
- [S4] H. Wang *et al.*, *Phys. Rev. Lett.* **103**, 200404 (2009).
- [S5] M. Hofheinz *et al.*, *Nature* **459**, 546 (2009).
- [S6] G. Lindblad, *Commun. Math. Phys.* **48**, 119 (1976).
- [S7] D. Leibfried *et al.*, *Phys. Rev. Lett.* **77**, 4281 (1996).
- [S8] D. F. Walls and G. J. Milburn, *Phys. Rev. A* **31**, 2403 (1985).